

## Architecture design of TiO<sub>2</sub> with Co-doped CdS quantum dots photoelectrode for water splitting

Fatih TEZCAN<sup>1,2</sup>, Abrar AHMAD<sup>2,3</sup>, Gülfeza KARDAŞ<sup>2\*</sup>

<sup>1</sup>Department of Chemistry and Chemical Process Technology, Vocational School of Technical Sciences at Mersin Tarsus Organized Industrial Zone, Tarsus University, Mersin, Türkiye

<sup>2</sup>Department of Chemistry, Faculty of Arts and Science, Çukurova University, Adana Türkiye

<sup>3</sup>Department of Chemistry, Quaid-i-Azam University, Islamabad, Pakistan

Received: 15.04.2023 • Accepted/Published Online: 30.09.2023 • Final Version: 31.10.2023

**Abstract:** Photoelectrochemical hydrogen production is a critical key to solving the carbon-zero goal of countries due to renewable sources of solar light and combustion products of hydrogen-only water. Here, an architecture design for an n-type nano rosettes-rod TiO<sub>2</sub> (RT) surface using CdS and Co-doped CdS quantum dots (QDs) is carried out utilizing the SILAR (simple ionic layer adsorption and reaction) method. Furthermore, the photocatalytic behaviour of Co-doped CdS QDs SILAR cycles deposition is investigated in various cycles, including 5, 8, 10, and 12. The FESEM, Raman XRD, Uv-Vis spectrometer, and vibration modes are used to evaluate the photoelectrode surface structure, crystal structure, and solar light absorption, respectively. FESEM images and XRD pattern revealed successive CdS QDS and Co-doped CdS QDs deposition on the RT boundary and rising SILAR cycles of Co-doped CdS QDs lead to further coverage of RT surface. UV-vis spectrometer indicated shifting solar light absorption to the visible region by applying more SILAR cycles of Co-doped CdS QDs deposition. The electrochemical parameters obtained from EIS showed total polarization resistance ( $R_p$ ) of the RT electrode dramatically decreased with 10 SILAR cycle Co-doped CdS QDs deposition (5093  $\Omega$  cm<sup>2</sup> and 617  $\Omega$  cm<sup>2</sup>). Linear sweep voltammetry (LSV) and chronoamperometric photocatalytic performance measurements indicated Co-doped CdS QDs on RT extremely enhanced photoresponse under solar irradiation and 10 SILAR cycle Co-doped CdS QDs improved photocurrent density about fourfold according to blank RT electrode.

**Key words:** TiO<sub>2</sub>, hydrogen production, photoanode, CdS QDs

### 1. Introduction

The intensive use of fossil-based resources in energy production for centuries has brought us to irreversible climate change [1–3]. At this level, countries have been announcing short-term and long-term carbon-zero action plans [4,5]. Action plans are created within environmentally friendly energy production and sustainability using renewable energy sources. According to this perspective, solar energy is the most critical potential in renewable energy sources. Solar energy can be transformed into electrical or direct photon energy. Photoelectrochemical hydrogen gas production uses photon energy from direct sunlight and applies bias potential by water splitting [6–9].

In the literature, the various semiconductors have been studied in the production of photoelectrochemical hydrogen gas such as ZnO [10,11], WO<sub>3</sub>[12,13], Cu<sub>2</sub>O [14,15], CuO [16–18], and TiO<sub>2</sub> [19–22]. TiO<sub>2</sub>, an n-type semiconductor, is widely preferred because it can be easily synthesized, modified in various morphologies, is chemically stable and is eco-friendly [23]. However, the absorption of TiO<sub>2</sub> in the UV region causes its utilization from sunlight to be relatively low [24]. Surface modifications on TiO<sub>2</sub> have been performed to improve solar light efficiency by shifting to the solar spectrum's visible region. Heterostructure application is mainly conducted on wide ( $E_g$ ) semiconductors by low  $E_g$  bandgap semiconductors [25–27]. A n-type semiconductor CdS, which can be synthesized as quantum dots (QDs), is widely preferred for constructing heterostructures in electrodes with large  $E_g$  values [28–30]. Furthermore, the absorption of CdS QDs performs with multiple excitations to solar-driven electron production in photocatalytic applications [31]. Therefore, electron transfer to wide  $E_g$  electrode can be enhanced with CdS QDs heterostructure. In addition, Mn, Cu, and Co metals doped to CdS QDs can be promising to improve photocatalytic performance [32–36]. Especially, many papers published about Mn-doped CdS QDs due to the increase of electron/hole lifetime for electron transition among broad band

\* Correspondence: gulfeza@cu.edu.tr

gap semiconductor energy levels for solar cells and photoelectrochemical cells [37,38]. Although CdS QDs modified TiO<sub>2</sub> application is more studied, Co-doped CdS QDs application is limited to solar and photoelectrochemical cells, especially on the TiO<sub>2</sub> substrate. For instance, Zou and co-workers [39] studied CdS/Co-doped CdSe electrodes on solar cells, suggesting Co-doping to CdSe, dropping the recombination of electron-hole, thus enhancing cell efficiency. Meng et al. [40] synthesized Co-doped carbon quantum dots on CdS nanorods (NRs) with various loading by hydrothermal deposition method for photocatalytic hydrogen production. It demonstrated exceptional photocatalytic activity due to the superior synergistic consequence between the Co nanoparticles and the carbon quantum dots. Co-doped CdS nanoparticles may generate a redshift, according to Thambidurai and colleagues [41], the chemical precipitation method produced CdS quantum dots. In the current study, we studied the design of a three-dimensional RT surface architecture using CdS QDs and Co-doped CdS QDs with the procedure of the simple ionic SILAR, which is inexpensive and fast to implement because it has no connection to a device and is extremely basic. Additionally, the photocatalytic behavior of Co-doped CdS QDs SILAR cycles deposition is investigated in various cycles, covering 5, 8, 10, and 12.

## 2. Materials and methods

### 2.1. Materials

Ti(OC<sub>4</sub>H<sub>9</sub>)<sub>4</sub> (97%), TiCl<sub>4</sub> (≥99.0%), Cd(NO<sub>3</sub>)<sub>2</sub>·4H<sub>2</sub>O (98%), (CH<sub>3</sub>COO)<sub>2</sub>Co·4H<sub>2</sub>O (99.0%), Na<sub>2</sub>S·9H<sub>2</sub>O (≥98.0%), HCl (37%), Na<sub>2</sub>SO<sub>3</sub> (95%), C<sub>3</sub>H<sub>6</sub>O (99.5%) C<sub>2</sub>H<sub>5</sub>OH (99.9%) were utilized without any further purification. The photocatalyst was synthesized on a Fluorine-doped tin oxide (FTO, ~8 Ω/Sq). The FTO working electrode was cleaned in the ultrasonic bath using a detergent solution, C<sub>3</sub>H<sub>6</sub>O, C<sub>2</sub>H<sub>5</sub>OH, and distilled water for a total of 10 min respectively.

### 2.2. Synthesis of the nano rosettes-rod TiO<sub>2</sub>

Synthesis of 3D nano rosettes-rod TiO<sub>2</sub> (RT) consists of two synthesis procedures according to a previous study by hydrothermal deposition method [42]. The first step is 1D TiO<sub>2</sub> hydrothermally synthesis by an earlier applied procedure. Concentrated HCl and distilled water were gradually mixed with similar volume and solution with constant stirring for 5 min. Ti(OC<sub>4</sub>H<sub>9</sub>)<sub>4</sub> was slowly put in solution, which was poured into a Teflon-lined stainless steel autoclave that previously replaced FTO substrates (surface area of 1 cm<sup>2</sup>). The synthesis of TiO<sub>2</sub> was conducted for 12 h at 150 °C in an oven by hydrothermal deposition. After deposition, electrodes were cleaned repeatedly with distilled water and C<sub>2</sub>H<sub>5</sub>OH before being dried in an electric oven at 60 °C. The electrodes were then heated in the furnace for an h at 500 °C.

In the second step, RT was obtained from the synthesis TiO<sub>2</sub> electrode. An autoclave at 100 °C for one h with a concentrated TiCl<sub>4</sub> solution. The same quantity of strong HCl and distilled water were added and stirred for 5 min. Step-by-step pours of concentrated TiCl<sub>4</sub> were performed, and the mixture was stirred once again for a duration of five min. Then the solution was replaced in an autoclave, which previously added TiO<sub>2</sub> electrode. The hydrothermal deposition was carried out in an autoclave for three h at 150 °C. The electrodes were washed with distilled water and ethyl alcohol before being heated to 60 °C. Finally, RT was heated for one h at a temperature of 500 °C.

### 2.3. Synthesis of Co-doped CdS on RT

CdS QDs and Co-doped CdS QDs were synthesized by the SILAR method. Initially, the samples were immersed in 0.1 M Cd(NO<sub>3</sub>)<sub>2</sub>·4H<sub>2</sub>O for 5 min, allowing Cd<sup>2+</sup> to diffuse to the RT surface and adsorb there. The RT sample was then removed from the solution and rinsed with distilled water to remove extra Cd<sup>2+</sup> cation. CdS QDs were produced by allowing the S<sup>2-</sup> anion to adsorb on the Cd<sup>2+</sup> terminated RT surface after the sample was exposed to 0.1 M Na<sub>2</sub>S·9H<sub>2</sub>O for 5 min, it is represented as RTC. The RTC sample was washed with distilled water and dried with an N<sub>2</sub> purge. The technique described above is known as a SILAR cycle. Co dopant in CdS QDs synthesis was performed in (CH<sub>3</sub>COO)<sub>2</sub>Co·4H<sub>2</sub>O-Cd(NO<sub>3</sub>)<sub>2</sub>·4H<sub>2</sub>O precursor solution. According to the experimental setup, both Co<sup>2+</sup> and Cd<sup>2+</sup> cations chemically adsorb to S<sup>2-</sup> on the RT surface. The SILAR cycles 5, 8, 10, and 12 were referred to as RTCCo\_xCy (where x varies regarding 5, 8, 10, and 12 cycles).

### 2.4. Characterization of the Photoelectrode

The crystal structure and hkl parameters of the prepared electrodes were characterized using an X-ray diffraction (XRD) pattern (Malvern PANalytical Empyrean). The surface structure was investigated using a scanning electron microscope (FEI Quanta 650 Field Emission SEM). The vibration modes of the semiconductor were studied at 532 nm excitation by Raman spectrophotometer (Renishaw InVia Qontor). A Uv-vis spectrometer (Agilent, Cary 7000) was utilized to obtain the optical absorption spectra of obtained photoelectrodes to characterize samples' absorption behaviour and band gap (Eg).

### 2.5. Photoelectrochemical test

The photocatalytic performances were carried out using the widely used three-electrode systems. The reference electrode, working electrode, and counter electrode are saturated Ag/AgCl (3 M KCl), the synthesis electrodes, and a Pt sheet (2 cm<sup>2</sup>), respectively. There were 0.1 M Na<sub>2</sub>SO<sub>3</sub> and 0.1 M Na<sub>2</sub>S in the solution. The CHI 660D electrochemical analyser was

used to conduct linear sweep voltammetry (LSV), electrochemical impedance spectroscopy (EIS), and Mott-Schottky experiments. The LSV measurement varied from  $-1.2$  to  $0.6$  V (vs. Ag/AgCl) at a scan rate of  $5 \text{ mV s}^{-1}$ . As the irradiation source of  $100 \text{ mW cm}^{-2}$ , a solar simulator (Sunlite TM sun Simulators, AM 1.5 filter) was utilized. EIS measurements were performed between  $10^{-1}$  and  $10^5$  Hz at  $0.3 \text{ V}_{\text{RHE}}$  over-potential,  $5 \text{ mV}$  in amplitude, and under  $100 \text{ mW cm}^{-2}$ . EIS results were fitted with ZView software to derive electrochemical parameters.

Chronoamperometric measurement (j-t) was performed using a chopped technique interval of 20 seconds light at  $0.3 \text{ V}$  (vs RHE) over-potential for 5 min. Mott-Schottky experiments were taken in the  $-0.4$ – $0.2 \text{ V}$  (vs. RHE) range, with a  $5 \text{ mV}$  amplitude at  $500 \text{ Hz}$  frequency and no light circumstances. The reference hydrogen electrode (RHE) was normalized at the photocatalytic measured potential vs. Ag/AgCl reference electrode at the photocatalytic measured potential. The following equation was used to calculate the overall potential of the water-splitting reaction vs RHE [40];

$$E_{\text{RHE}} = E_{\text{Ag/AgCl}} + E_{\text{Ag/AgCl}}^{\circ} + 0.059\text{pH} \quad (1)$$

Herein,  $E_{\text{RHE}}$  is converted potential vs. RHE,  $E_{\text{Ag/AgCl}}$  is the obtained potential vs. Ag/AgCl reference electrode, and  $E_{\text{Ag/AgCl}}^{\circ}$  is  $0.197 \text{ V}$  for  $3.0 \text{ M KCl}$  at  $25 \text{ }^{\circ}\text{C}$ .

An applied bias photon-to-current efficiency ( $\eta$ ) of the samples, that is, the photoconversion efficiency, was calculated according to the following equation:

$$\eta(\%) = J_{\text{ph}} \frac{1.23-V}{p_{\text{total}}} \times 100 \quad (2)$$

Where,  $J_{\text{ph}}$  is the obtained photocurrent density,  $V$  is the over-potential vs RHE, and  $p_{\text{total}}$  is used solar light ( $100 \text{ mW cm}^{-2}$ ).

### 3. Results

#### 3.1. Photoelectrode characterization

The crystal structure and phase planes of the samples were measured with  $2\theta$  values ranging from  $20^{\circ}$  to  $80^{\circ}$  by XRD pattern. The XRD pattern of samples is depicted in Figure 1. The pattern of pristine RT exhibits  $2\theta$  values and hkl are  $27.20^{\circ}$  (110),  $36.01^{\circ}$  (101),  $38.85^{\circ}$  (200),  $41.14^{\circ}$  (111),  $44.26^{\circ}$  (210),  $54.28^{\circ}$  (211),  $56.61^{\circ}$  (220),  $62.83^{\circ}$  (002),  $65.47^{\circ}$  (221), and  $69.01^{\circ}$  (301). The prepared sample is the tetragonal rutile phase of  $\text{TiO}_2$  (pdf card no: 98-016-8140) [43]. Furthermore,

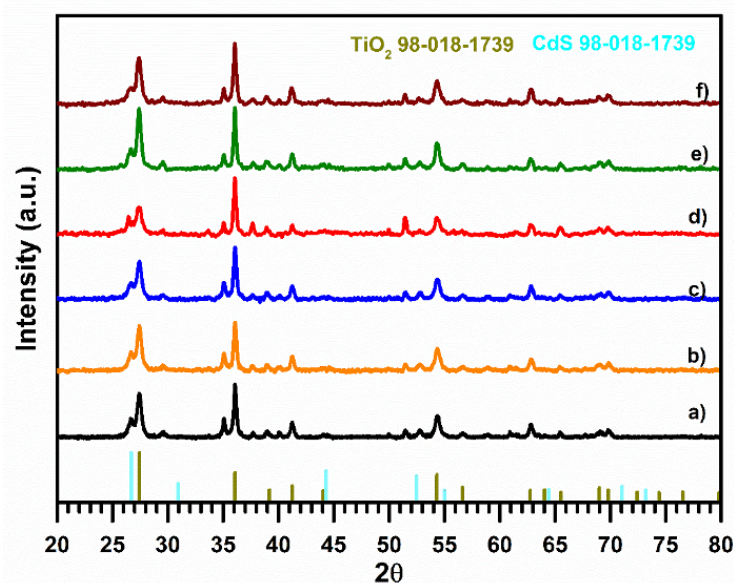


**Figure 1.** XRD pattern of (a) RT, (b) RTC, (c) RTCCo\_5Cy (d) RTCCo\_8Cy, (e) RTCCo\_10Cy, and (f) RTCCo\_12Cy.



the main peaks  $27.20^\circ$ ,  $36.01^\circ$ , and  $54.28^\circ$  indicate successively obtained RT [44,45]. According to previous studies, CdS QDs synthesis with the SILAR method commonly obtained the cubic phase of CdS [46,47]. The main distinctive  $2\theta$  peaks of CdS are  $26.72^\circ$  and  $44.33^\circ$ , associated with the (111) and (202) hkl parameters. But these peaks overlap with  $27.40^\circ$  and  $44.04^\circ$  the rutile phase of  $\text{TiO}_2$ , resulting in distinct  $2\theta$  values incredibly similar to the characteristic peaks of the sample and causing identifying difficulty of  $2\theta$  peaks [48,49]. Additionally, a considerable peak difference is unavailable in the XRD pattern with the addition of  $\text{Co}^{2+}$  and various SILAR cycles. It can be concluded that the nanoparticles adsorb on  $\text{TiO}_2$ , leading to few amount depositions on  $\text{TiO}_2$  and causing under the measurement detection limit/overlap peak observation. Therefore, FESEM, Raman and Uv-vis analysis were performed to define the Co doped CdS QDs on the RT surface.

The surface morphology of RT RTC, and various RTCCo photoelectrodes are given in Figure 2. According to FESEM images, the nano rosettes clearly observe with the applied two synthesis setup procedure. RT consist of tiny nanorods play acting as a structural component. Therefore, at the second step of the synthesis,  $\text{TiO}_2$  grow up on the tip of the

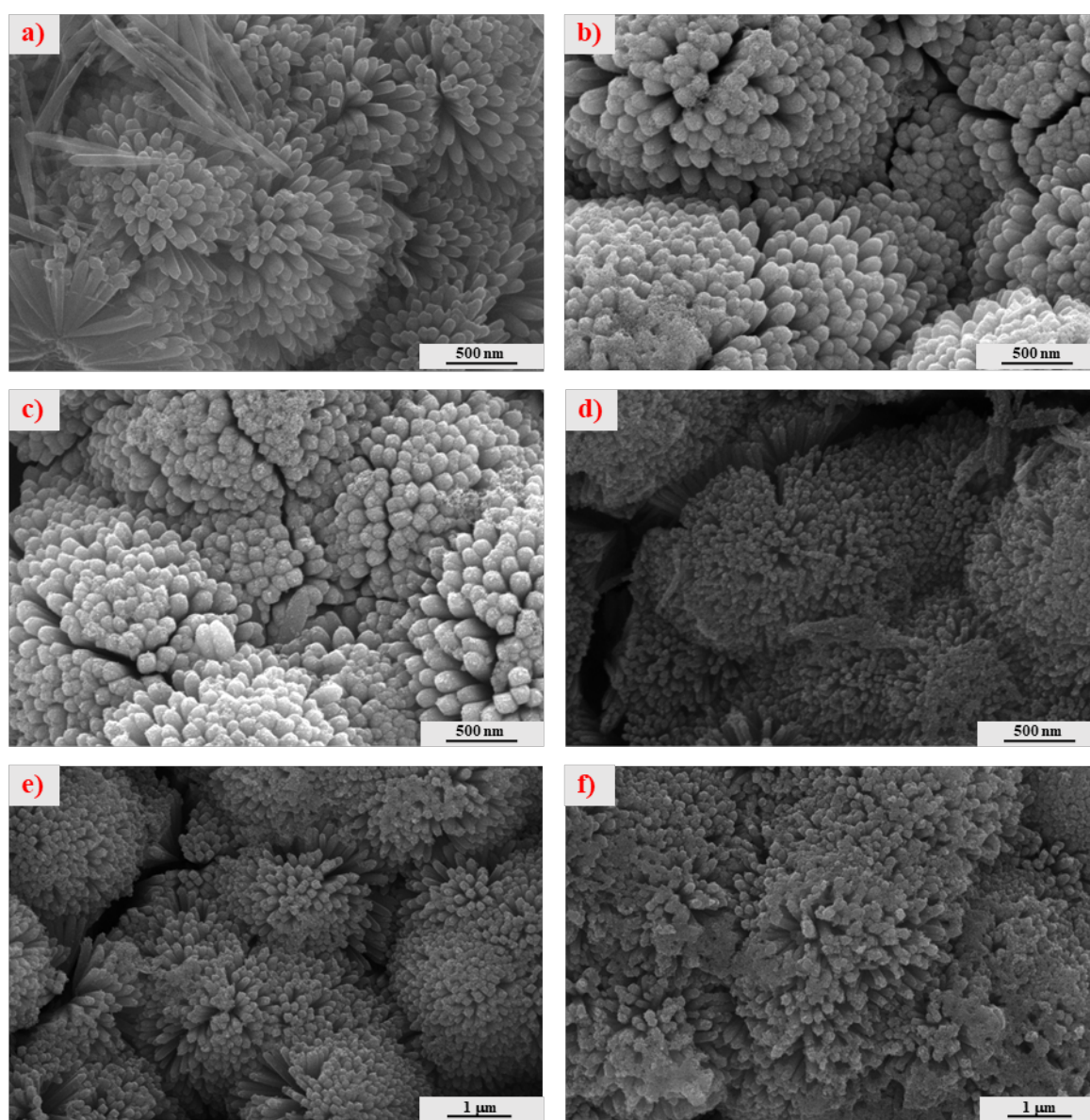


**Figure 2.** FESEM images (a) RT, (b) RTC, (c) RTCCo\_5Cy, (d) RTCCo\_8Cy, (e) RTCCo\_10Cy, and (f) RTCCo\_12Cy.

nanorod, enabling active surface boundary to adsorb Co-doped CdS QDs and enhancing solar light efficiency. In Figure 2 (b), CdS deposition causes QDs accumulation over RT, and its surface converts rougher surface structure. Furthermore, the nanoparticles are perfectly deposited on the RT surface and increasing SILAR cycle enhanced Co-doped CdS QDs deposition. Also, Co-doped CdS nanoparticles further attached the tip of RT at the 12 cycles, causing clog RT active surface and decreasing the RT surface area to performing the photoelectrochemical process (in Figure 2(b)).

Raman measurements to define vibration modes of CdS QDs and Co dopant CdS QDs on RT and further probe the content of the photoelectrode were taken between 100 and 1200  $\text{cm}^{-1}$ . Raman spectrums of the photoelectrodes are given in Figure 3. The pristine RT gives 237, 446, and 612  $\text{cm}^{-1}$ , associated with the main three  $B_{1g}$ ,  $E_g$ , and  $A_{1g}$  vibration modes of RT [50]. Both  $E_g$  and  $A_{1g}$  are related to the active mode, however,  $B_{1g}$  vibration mode corresponds to multiple phonon vibrations. In addition, in terms of RTCCo\_5Cy photoanode, deposition of CdS on RT can be clearly confirmed with two peaks at 300  $\text{cm}^{-1}$  and 606  $\text{cm}^{-1}$ , connected to the first order longitudinal optical phonon (1LO) and second order longitudinal optical phonon (2LO) on active Raman mode [51,52]. As seen in the Raman spectrum, 2LO of the CdS peak overlapped with  $A_{1g}$  of  $\text{TiO}_2$ , but the 1LO peak obviously appeared at 300  $\text{cm}^{-1}$ , suggesting deposition of CdS.

A UV-visible spectrometer was used to examine the solar light absorption behaviour and band gap ( $E_g$ ) energy of electrodes. The solar absorption spectrum ranges from 380–800 nm of the pristine RT and various RTCCo electrodes are given in Figure 4. Commonly, the  $\text{TiO}_2$  electrode absorbs light in the ultraviolet region [53]. RT absorption inset value is about  $\sim 410$  nm, and the  $E_g$  value is 3.05, consistent with previous  $\text{TiO}_2$  studies. As CdS QDs deposition on the RT surface, the absorption inset is shifted from ultraviolet to the visible region at about 520 nm. Furthermore,  $\text{Co}^{2+}$  doped CdS QDs also is shifted further visible region, suggesting  $\text{Co}^{2+}$  replaced among both valence and conduction band energy levels of CdS QDs and supplied further electron transfer [54,55]. Also, adding  $\text{Co}^{2+}$  in the CdS QDs, can be concluded that the  $\text{Co}^{2+}$  loading quantity of QDs enabled to increase in the deposition of QDs on the RT boundary. According to various RTCCo electrode spectrum, absorbance is shifting visible region with increasing SILAR cycles RTCCo electrodes and RTCCo\_12Cy demonstrates absorption inset behaviour in the more visible region. It suggests that increasing the SILAR cycle enables further  $\text{Co}^{2+}$  loading quantity of CdS QDs and improves electron transportation along with the CdS energy level. In addition,  $E_g$  values of samples are calculated by Tauc's following equation;

$$(\alpha h\nu)^{1/r} = A (h\nu - E_g) \quad (3)$$

Herein,  $\alpha$  is the absorption coefficient,  $h$  is a Planck constant,  $\nu$  is frequency,  $r$  vis the direct band transition ( $r = 1/2$ ), and  $A$  is the experimental constant. The Uv-vis absorption curve converts to  $(\alpha h\nu)^2$  versus  $h\nu$ .  $E_g$  value is obtained by extrapolating the curve to the x-axis of the curve drawing, and Tauc's plots are given in Figure 4 (b). According to  $E_g$  values, Co-doped CdS QDS enable lower  $E_g$  value compared with bare CdS QDs electrode, and the various Co-doped CdS QDs

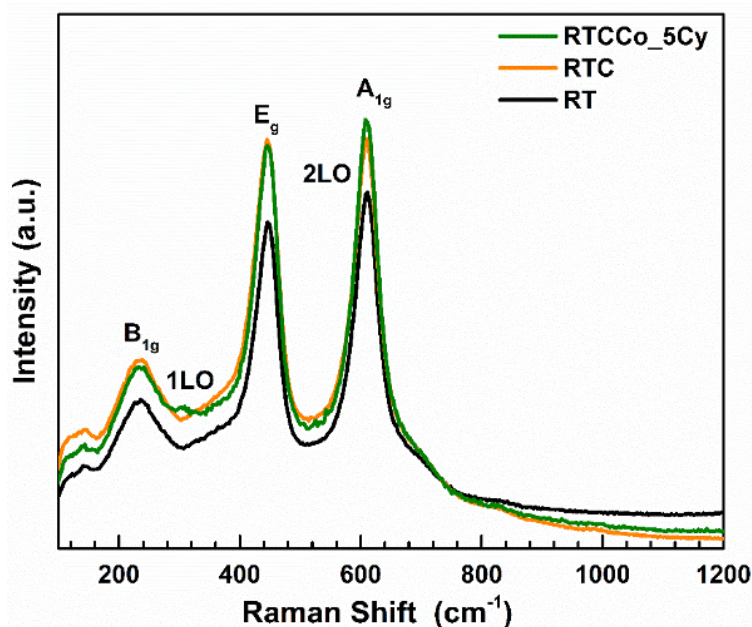


Figure 3. Raman spectrum of RT, RTC, RTCCo\_5Cy.

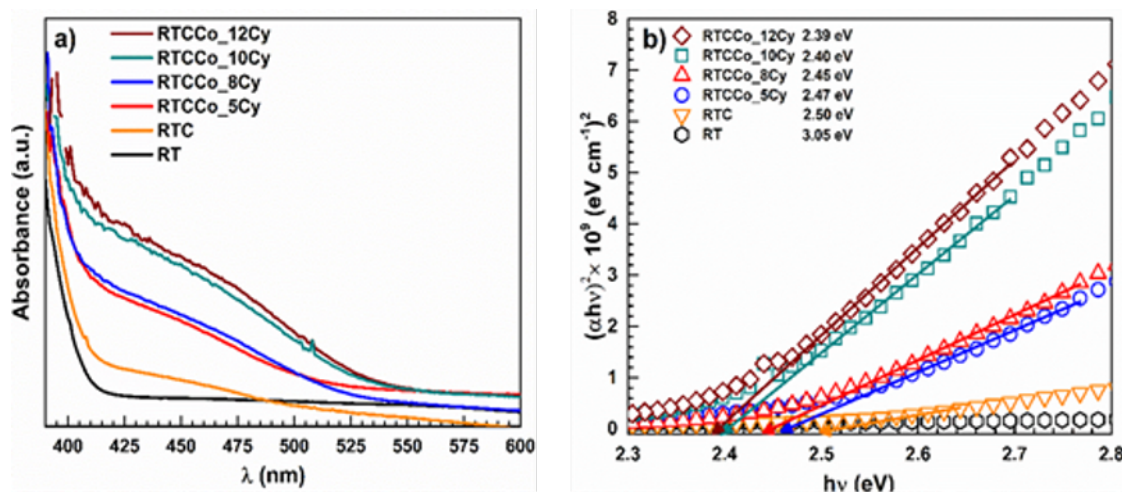


Figure 4. Uv-Vis spectrum (a) and Tauc plot (b) of the photoelectrodes.

$E_g$  is decreased with increasing SILAR deposition cycle numbers. It indicates that in large amounts deposition caused to boost of the recombination rate of photogenerated electron-hole pairs.

### 3.2. Photoelectrochemical performance

LSV, ABPE and  $j-t$  were conducted to enlighten on the sample's photocatalytic activity for solar-driven water splitting to produce hydrogen. The LSV measurements were performed  $-1.2-0.6$  V (vs. Ag/AgCl) under the chopped method, which is given in Figure 5 (a). The chopped procedure clearly indicates zero current density and rapid current density increasing, dark and light conditions, respectively. It could be concluded that all the obtained samples act as a semiconductor under photo-induced by solar light. The electrochemical water electrolysis overall potential is about 1.23 V (vs. RHE), which is critical to distinguish the photochemical performance of electrodes. Therefore, As comparing current density at the 1.23 V (vs. RHE), RT, RTC, RTC\_5Cy, RTC\_8Cy, RTC\_10Cy and RTC\_12Cy, are  $0.377$  mA cm<sup>-2</sup>,  $0.522$  mA cm<sup>-2</sup>,  $1.013$  mA cm<sup>-2</sup>,  $1.284$  mA cm<sup>-2</sup>,  $1.534$  mA cm<sup>-2</sup> and  $1.647$  mA cm<sup>-2</sup>, respectively. It indicates that i) CdS QDs enhanced photo response of RT as a result of further photo-excited electron of CdS giving to RT energy level, ii) Co-doped CdS QDs enhances photocatalytic activity compared to without Co-doped CdS QDS, due to Co<sup>2+</sup> doped enable further rapid charge recombination on CdS QDs, iii) increasing SILAR cycle number improve catalytic activity on water splitting, but the current density of RTC\_12Cy decreases relating excess Co-doped CdS QDs loading blocked of active surface on RT surface.

In the photoelectrochemical setup, hydrogen production was obtained on the photoelectrode surface by photoelectrochemical reaction, which is associated with both bias potential and solar irradiation applied to the faradaic process. Therefore, one of the most photoconversion efficiency of the electrode is ABPE, given in Figure 5 (b). The measured maximum photoconversion efficiency % of RT, RTC, RTCCo\_5Cy, RTCCo\_8Cy, RTCCo\_10Cy and RTCCo\_12Cy, are 0.221, 0.334, 0.742, 0.799, 1.053, and 0.888, respectively. The results indicate that RT photoconversion efficiency % is not only enhanced with CdS QDS but also with various cycles Co-doped CdS QDs electrodes are further improved photocatalytic activity on water splitting. It relates to Co-doped enabling electrical conductivity, increasing RT electrode and leading to more electron transfer among CdS QDs energy level [56]. Consequently, RTCCo\_10Cy demonstrates the utmost photoconversion efficiency %, and Co-doped CdS QDs at 12 cycles lead to decreasing photoconversion efficiency % value. It suggests increasing the number of cycles causing the block to active side on the RT surface and decreasing imposing solvated ion at the electrode/electrolyte boundary by the photoelectrochemical process.

The chronoamperometric measurement was performed to photo-durability under a bias 0.3 V (vs. RHE) potential with the chopped method, as shown in Figure 5 (c). The light-off condition demonstrates zero current density due to inaccessible electron transition among semiconductor energy levels. The samples perform abrupt current density increasing and achieve a steady state under light-on conditions, resulting in rapid electron decay from VB to CB band and electron/hole recombination procedure, respectively. As seen in Figure 5 (c), all samples are performed durable photoresponse under the chopped method after about two s for 300 s. Furthermore, the chronoamperometric curve implies that Co-doped among various cycles CdS QDs electrodes RTCCo\_10Cy shows the highest current density, which conforms with the LSV results.

Commonly, EIS measurement prefers to recognize electrode/electrolyte interface resistances, electron/hole



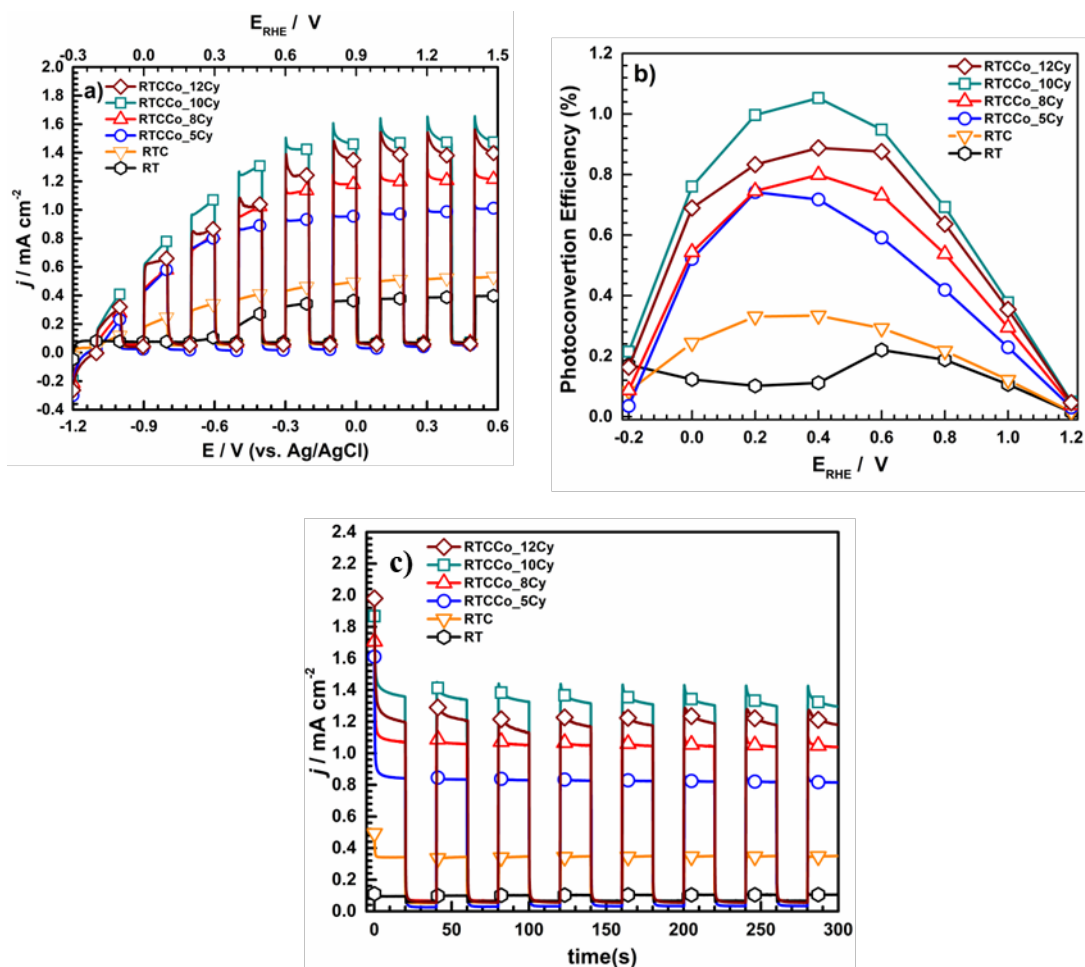


Figure 5. LSV results (a) photoconversion efficiency (b) and chronoamperometric measurement of photoelectrodes.

recombination process, and photoelectrochemical charge transfer [57–59]. To understand resistance sources connected with the photoelectrochemical reaction, EIS measurements were carried out with an applied bias potential of 0.3 V (vs. RHE) under 100 mW cm<sup>-2</sup>. Nyquist and phase angle-frequency plots of the photoelectrodes are shown in Figure 6(a and b). According to the Nyquist plot, electrodes display three depressed loops, two of which are in the higher frequency region and one of which is in the lower frequency region. Based on the EIS theory, a smaller loop denotes a lower resistance, whereas a larger loop leads to a higher resistance at the electrode-electrolyte double layer. Both CdS QDs and Co doped CdS QDs deposition leads decreasing in depressed loops RT, suggesting photocatalyst loading on RT reduced various resistances sources on O<sub>2</sub> evolution reaction (OER). Additionally, when compared to other samples, RTCCo\_10Cy represents the lowest loop, which enhances the electrical conductivity of the Co-doped CdS QDs and provides more electrons from the VB to CB energy level. Phase angle-frequency plots of the samples are given in Figure 6 (b). According to phase angle-frequency plots, all samples indicate three-time constants from higher to lower frequency. The last point of the curve on the phase angle-frequency plot indicates the  $R_f$  and indicator coverage of the electrode at the lower frequency. The applying Co-doped process assists in decreasing of  $R_f$  value, resulting in electron transportation among energy levels of Co, providing reduce the speed of the recombination process and the electrons remain for a slower time in the Co orbitals at the lower frequency region. Furthermore, Co-doped provides decreasing in maximum phase angle on RT and RTC electrodes.

EIS measurement was fitted to calculate electrochemical parameters by a suggested electrical equivalent circuit (Figure 6). The electrochemical parameters are listed in Table 1, including various resistances and constant phase elements (CPE). The electrical equivalent circuit diagram demonstrates that the samples consist of three CPE.  $R_1$  is the charge transfer

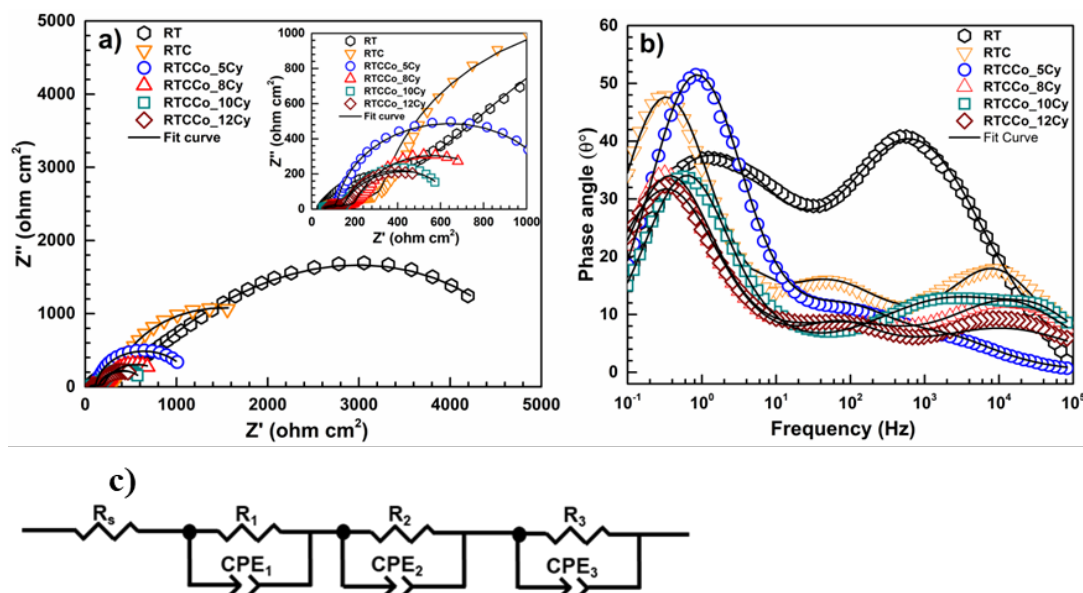


Figure 6. Nyquist plot (a), phase angle-frequency plot (b), and suggested electrical equivalent circuit (c).

Table 1. Electrochemical parameters of photoelectrode by fitted Zview software.

Photoelectrode	$R_1$ $\Omega$ $\text{cm}^2$	$C_{\text{CPE1}} \times 10^{-4}$ $\Omega^{-1}\text{s}^n\text{cm}^{-2}$	$R_2$ $\Omega$ $\text{cm}^2$	$C_{\text{CPE2}} \times 10^{-4}$ $\Omega^{-1}\text{s}^n\text{cm}^{-2}$	$R_3$ $\text{cm}^2$	$\Omega$	$C_{\text{CPE3}} \times 10^{-4}$ $\Omega^{-1}\text{s}^n\text{cm}^{-2}$	$R_p$ $\Omega$ $\text{cm}^2$
RT	435	0.302	1698	3.992	2960	1.481	5093	
RTC	78	0.578	194	1.678	2401	5.997	2673	
RTCCo-5Cyc	45	2.334	13	46.141	1050	6.101	1108	
RTCCo-8Cyc	71	3.080	66	51.980	725	11.417	862	
RTCCo-10Cyc	98	4.173	8	53.181	511	12.011	617	
RTCCo_12Cyc	33	1.582	46	48.454	580	21.414	638	

resistance ( $R_{ct}$ ) (at higher frequency region),  $R_2$  is the barrier resistance ( $R_b$ ), and  $R_3$  is the film resistance ( $R_f$ ) (at lower frequency). It refers to  $R_s$ , which represents to the solution resistance (related uncompensated resistance). The sum of all resistance in the photoelectrochemical cell is called the polarization resistance ( $R_p$ ), including  $R_{ct}$ ,  $R_b$ , and  $R_f$ . According to Table 1, when compared to samples of undoped CdS and unmodified RT, the  $R_p$  values of Co-doped CdS QDs modified RT are the lowest. It suggests that Co is doped on the surface, enabling decreasing resistance on OER process sources at the electrode/electrolyte interface. Furthermore, RTCCo\_10Cy demonstrates the lowest  $R_p$  among RTCCo electrodes, suggesting that the optimum Co-doped in the CdS QDs is 10 SILAR cycles, leading to imposed active surface boundary to photocatalytic reaction. Increasing of SILAR cycles to 12 caused to blocked catalytic surface and rising  $R_f$  value on the OER process.

A semiconductor/electrode interface can be measured by Mott-Schottky measurement. Figure 7 demonstrates the Mott-Schottky plot of samples ranging from  $-0.2$  and  $0.4$  V. A negative slope and positive slope indicate a p-type and an n-type semiconductor, respectively. As seen in Figure 7, all samples show an n-type semiconductor. The theory of capacitance provides a calculation of charge carrier density ( $N_D$ ) at the electrochemical double layer by using the following Mott-Schottky equation [60];

$$\frac{1}{C^2} = \frac{2}{q\epsilon\epsilon_0 N_D} \left[ V - V_{fb} - \frac{K_B T}{q} \right] \quad (4)$$



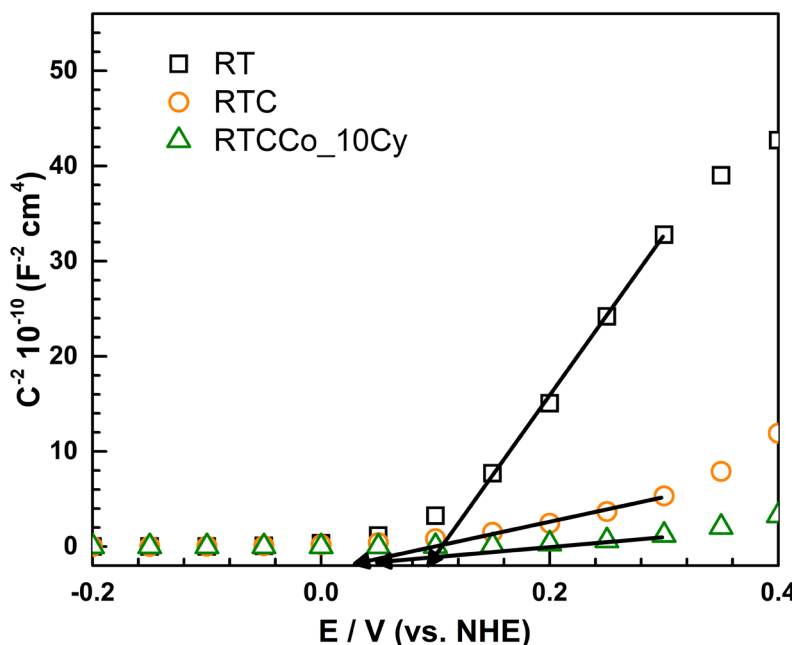


Figure 7. The Mott-Schottky plots of photoelectrodes.

Herein  $q$  is the electron charge,  $C$  is the capacitance at the electrochemical double layer,  $\epsilon_0$  is the permittivity in a vacuum,  $\epsilon$  is the dielectric constant,  $k_b$  is the Boltzmann constant,  $V$  is the applied bias potential,  $V_{fb}$  is the flat band potential and  $T$  is the condition temperature. The  $V_{fb}$  value of the sample calculates with an extrapolation curve to the x-axis. Furthermore, the electron density  $N_D$  obtains on curve slope ( $S$ ) by following equation [61];

$$N_D = \frac{2}{q\epsilon\epsilon_0 S} \quad (5)$$

The  $N_D$  and  $V_{fb}$  of samples are given in Table 2. The  $N_D$  is associated with the steady state of the semiconductor, performing no charge depletion or band bending. According to obtained  $N_D$ , RTCCo\_10Cy performs the utmost value, suggesting provides further electron transportation to photoelectrochemical water splitting at the double layer. Increasing  $C$  corresponds to the charging of electrode/electrode boundary to nonfaradaic processes. Therefore, the  $C$  value is the lowest at 0.4 V compared to RT and RTC. The  $V_{fb}$  corresponds to the low velocity of electron/hole recombination at the energy levels of the semiconductor. By way of the  $V_{fb}$  further negative, electron/hole recombination rate decreases and performs catalytic photoresponse. As seen in Table 2, RTCCo\_10Cy shows more negative  $V_{fb}$  value, concluding high photocatalytic performance on the OER process.

#### 4. Discussion

By using the SILAR cycle deposition process, we have successfully produced the nanoparticles of CdS QDs and Co-doped CdS QDS on RT. The cycle effect of SILAR deposition was analysed in detail on the crystal structure, surface morphology, light absorption, and photoelectrochemical performance. The XRD patterns confirmed distinctive  $20^\circ$  peaks of CdS are  $26.72^\circ$  and  $44.33^\circ$ . FESEM surface images showed that increasing SILAR cycles caused to enhancing deposition of Co-doped CdS QDS on RT and coverage to the active side of the boundary. EIS measurement revealed RTCCo\_10Cy's lowest loop compared to other samples, resulting in enhancing the electrical conductivity. Mott-Schottky measurement showed that all samples were an n-type semiconductor behaviour and the RTCCo\_10Cy electrode exhibited the major  $N_D$  and the most negative  $V_{fb}$ . The photoelectrochemical measurements revealed CdS QDs and Co doped CdS QDS enhanced photoelectrochemical response of RT and RTCCo\_10Cy the highest under solar irradiation. The present study demonstrates as an optimum Co doped CdS QDS SILAR deposition cycle is 10 cycles on RT photoelectrode revealing superior photocatalytic properties which can be applied to solar cells and other photocatalytic applications.

**Table 2.** Mott-Schottky parameters of photoelectrodes.

Electrodes	$V_{fb}$ ( $V_{RHE}$ )	$N_d \times 10^{18} \text{ cm}^{-3}$
RT	0.168	0.492
RTC	0.098	2.543
RTCCo_10 Cyc	0.120	14.603

**Acknowledgement and/or disclaimers, if any**

The authors gratefully acknowledge the support of Çukurova University's Scientific Research Projects Unit (FBA-2019-12171) and Turkey's Scientific and Technological Research Council (TUBITAK) 2216 Research Fellowship Program for Foreign Citizens.

**References**

- [1] Simpson NP, Mach KJ, Constable A, Hess J, Hogarth R et al. A framework for complex climate change risk assessment. *One Earth* 2021; 4 (4): 489-501. <https://doi.org/10.1016/j.oneear.2021.03.005>
- [2] Valentová A, Bostik V. Climate change and human health. *Military Medical Science Letters* 2021; 90 (2): 50. <https://doi.org/10.31482/mmml.2021.010>
- [3] Short JR, Farmer A. Cities and Climate Change. *Earth (Switzerland)* 2021; 2 (4): 1038-1045. <https://doi.org/10.3390/earth2040061>
- [4] Heffernan E, Pan W, Liang X, de Wilde P. Zero carbon homes: Perceptions from the UK construction industry. *Energy Policy* 2015; 79: 23-36. <https://doi.org/10.1016/j.enpol.2015.01.005>
- [5] Seto KC, Churkina G, Hsu A, Keller M, Newman PWG et al. From Low- To Net-Zero Carbon Cities- To Next Global Agenda. *Annual Review of Environment and Resources* 2021; 46: 377-415. <https://doi.org/10.1146/annurev-environ-050120-113117>
- [6] Li X, Zhao L, Yu J, Liu X, Zhang X et al. Water Splitting: From Electrode to Green Energy System. *Nano-Micro Letters* 2020; 12: 1-29. <https://doi.org/10.1007/s40820-020-00469-3>
- [7] Joy J, Mathew J, George SC. Nanomaterials for photoelectrochemical water splitting–review. *International Journal of Hydrogen Energy*, 2018; 43 (10): 4804-4817. <https://doi.org/10.1016/j.ijhydene.2018.01.099>
- [8] Mohsin M, Ishaq T, Bhatti IA, Maryam, Jilani A et al. Semiconductor Nanomaterial Photocatalysts for Water-Splitting Hydrogen Production: The Holy Grail of Converting Solar Energy to Fuel. *Nanomaterials* 2023; 13 (3): 546. <https://doi.org/10.3390/nano13030546>
- [9] Hota P, Das A, Maiti DK. A short review on generation of green fuel hydrogen through water splitting. *International Journal of Hydrogen Energy* 2023; 48 (2): 523-541. <https://doi.org/10.1016/j.ijhydene.2022.09.264>
- [10] Galdámez-Martínez A, Santana G, Güell F, Martínez-Alanis PR, Dutt A. Photoluminescence of ZnO nanowires: A review. *Nanomaterials* 2020; 10 (5): 857. <https://doi.org/10.3390/nano10050857>
- [11] Albiter E, Merlano AS, Rojas E, Barrera-Andrade JM, Salazar Á et al. Synthesis, characterization, and photocatalytic performance of ZnO-graphene nanocomposites: A review. *Journal of Composites Science* 2021; 5 (1): 4. <https://doi.org/10.3390/jcs5010004>
- [12] Tran VA, Nguyen TP, Le VT, Kim IT, Lee SW et al. Excellent photocatalytic activity of ternary Ag@WO<sub>3</sub>@rGO nanocomposites under solar simulation irradiation. *Journal of Science: Advanced Materials and Devices* 2021; 6 (1): 108-117. <https://doi.org/10.1016/j.jsamd.2020.12.001>
- [13] Tayebi M, Masoumi Z, Lee BK. Ultrasonically prepared photocatalyst of W/WO<sub>3</sub> nanoplates with WS<sub>2</sub> nanosheets as 2D material for improving photoelectrochemical water splitting. *Ultrasonics Sonochemistry* 2021; 70: 105339. <https://doi.org/10.1016/j.ultsonch.2020.105339>
- [14] Yu R, Chen Q, Li W, Yu X, Zhong Q. Decorating Cu<sub>2</sub>O with Ni-doped metal organic frameworks as efficient photocathodes for solar water splitting. *International Journal of Hydrogen Energy* 2023; 48 (45): 17065-17073. [doi.org/10.1016/j.ijhydene.2023.01.145](https://doi.org/10.1016/j.ijhydene.2023.01.145)
- [15] Yang L, Wang R, Chu D, Chen Z, Zhong F et al. BiVO<sub>4</sub> photoelectrodes for unbiased solar water splitting devices enabled by electrodepositing of Cu<sub>2</sub>O simultaneously as photoanode and photocathode. *Journal of Alloys and Compounds* 2023; 945: 169336. <https://doi.org/10.1016/j.jallcom.2023.169336>

- [16] Siavash Moakhar R, Hosseini-Hosseinabad SM, Masudy-Panah S, Seza A, Jalali M et al. Photoelectrochemical Water-Splitting Using CuO-Based Electrodes for Hydrogen Production: A Review. *Advanced Materials* 2021; 33 (33): 2007285. <https://doi.org/10.1002/adma.202007285>
- [17] de Brito JF, Tavella F, Genovese C, Ampelli C, Zanoni MVB et al. Role of CuO in the modification of the photocatalytic water splitting behavior of TiO<sub>2</sub> nanotube thin films. *Applied Catalysis B: Environmental* 2018; 224: 136-145. <https://doi.org/10.1016/j.apcatb.2017.09.071>
- [18] Baran Aydın E, Ateş S, Sığircık G. CuO-TiO<sub>2</sub> nanostructures prepared by chemical and electrochemical methods as photo electrode for hydrogen production. *International Journal of Hydrogen Energy* 2022; 47.10: 6519-6534. <https://doi.org/10.1016/j.ijhydene.2021.12.032>
- [19] Anantha Prabhu C, Silambarasan D, Sarika R, Selvam V. Synthesis and characterization of TiO<sub>2</sub>. *Materials Today: Proceedings* 2022; 64: 1793-1797. <https://doi.org/10.1016/j.matpr.2022.06.074>
- [20] Gupta SM, Tripathi M. A review of TiO<sub>2</sub> nanoparticles. *Chinese Science Bulletin* 2011; 56 (16): 1639-1657. <https://doi.org/10.1007/s11434-011-4476-1>
- [21] Li B, Wu S, Gao X. Theoretical calculation of a TiO<sub>2</sub>-based photocatalyst in the field of water splitting: A review. *Nanotechnology Reviews* 2020; 9 (1): 1080-1103. <https://doi.org/10.1515/ntrev-2020-0085>
- [22] Aydın EB, Sığircık G, Takci HAM. Antimicrobial properties and corrosion behavior of TiO<sub>2</sub>-NTs electrodes modified with Ag and ZnO nanorod in simulated body fluid solution. *Journal of Molecular Structure* 2021; 1240: 130569. <https://doi.org/10.1016/j.molstruc.2021.130569>
- [23] Zhang X, Zhang S, Cui X, Zhou W, Cao W et al. Recent Advances in TiO<sub>2</sub>-based Photoanodes for Photoelectrochemical Water Splitting. *Chemistry–An Asian Journal* 2022; 17 (20): 202200668. <https://doi.org/10.1002/asia.202200668>
- [24] Zallen R, Moret MP. The optical absorption edge of brookite TiO<sub>2</sub>. *Solid State Communications*, 2006; 137 (3): 154-157. <https://doi.org/10.1016/j.ssc.2005.10.024>
- [25] Liu H, Li D, Yang X, Li H. Fabrication and characterization of Ag<sub>3</sub>PO<sub>4</sub>/TiO<sub>2</sub> heterostructure with improved visible-light photocatalytic activity for the degradation of methyl orange and sterilization of E.coli. *Materials Technology* 2019; 34 (4): 192-203. <https://doi.org/10.1080/010667857.2018.1545391>
- [26] Ücker CL, Riemke F, Goetzke V, Moreira ML, Raubach CW et al. Facile preparation of Nb<sub>2</sub>O<sub>5</sub>/TiO<sub>2</sub> heterostructures for photocatalytic application. *Chemical Physics Impact* 2022; 4: 100079. <https://doi.org/10.1016/j.chphi.2022.100079>
- [27] My Tran N, Thanh Hoai Ta Q, Noh JS. Unusual synthesis of safflower-shaped TiO<sub>2</sub>/Ti<sub>3</sub>C<sub>2</sub> heterostructures initiated from two-dimensional Ti<sub>3</sub>C<sub>2</sub> MXene. *Applied Surface Science* 2021; 538: 148023. <https://doi.org/10.1016/j.apsusc.2020.148023>
- [28] Nandi P, Das D. ZnO/CdS/CuS heterostructure: A suitable candidate for applications in visible-light photocatalysis. *Journal of Physics and Chemistry of Solids* 2022; 160: 110344. <https://doi.org/10.1016/j.jpcs.2021.110344>
- [29] Jia Y, Zhang Y, Wei X, Guo T, Fan J et al. GaTe/CdS heterostructure with tunable electronic properties via external electric field and biaxial strain. *Journal of Alloys and Compounds* 2020; 832: 154965. <https://doi.org/10.1016/j.jallcom.2020.154965>
- [30] Guo X, Liu X, Yan J, Liu S. Heteroepitaxial growth of core-shell ZnO/CdS heterostructure for efficient and stable photocatalytic hydrogen generation. *International Journal of Hydrogen Energy* 2022; 47 (81): 34410-34420. <https://doi.org/10.1016/j.ijhydene.2022.08.032>
- [31] Sun WT, Yu A, Pan HY, Gao XF, Chen Q et al. CdS quantum dots sensitized TiO<sub>2</sub> nanotube-array photoelectrodes. *Journal of the American Chemical Society* 2008; 130: 1124-1125. <https://doi.org/10.1021/ja0777741>
- [32] Sivaranjani K, Sivakumar S, Dharmaraja J. Enhancement Photocatalytic Activity of Mn Doped CdS/ZnO Nanocomposites for the Degradation of Methylene Blue Under Solar Light Irradiation. *Advances in Materials Science* 2022; 22 (2): 28-48. <https://doi.org/10.2478/adms-2022-0006>
- [33] Muruganandam S, Anbalagan G, Murugadoss G. Optical and magnetic properties of PVP surfactant with Cu doped CdS nanoparticles. *Optik* 2017; 130: 82-90. <https://doi.org/10.1016/j.ijleo.2016.11.053>
- [34] Diaz-Grijalva OI, Berman-Mendoza D, Flores-Pacheco A, López-Delgado R, Ramos-Carrasco A et al. Cu-doped CdS thin films by chemical bath deposition and ion exchange. *Journal of Materials Science: Materials in Electronics* 2020; 31: 1722-1730. <https://doi.org/10.1007/s10854-019-02690-2>
- [35] Ibraheem F, Mahdy MA, Mahmoud EA, Ortega JE, Rogero C et al. Tuning Paramagnetic effect of Co-doped CdS diluted magnetic semiconductor quantum dots. *Journal of Alloys and Compounds* 2020; 834: 155196. <https://doi.org/10.1016/j.jallcom.2020.155196>
- [36] Gbashi KR, Muhi MAH, Jabbar AA, Mahmood NB, Hasan RF. Copper dopants impact enhanced behavior of Mn:Cu co-doped CdS nanocrystals (quantum dots) and their characteristics for optoelectronic applications. *Applied Physics A Process* 2020; 126.8: 628. <https://doi.org/10.1007/s00339-020-03801-1>
- [37] Ahmad A, Tezcan F, Yerlikaya G, Zia-ur-Rehman, Paksoy Het al. Solar light driven photoelectrochemical water splitting using Mn-doped CdS quantum dots sensitized hierarchical rosette-rod TiO<sub>2</sub> photoanodes. *Journal of Electroanalytical Chemistry* 2022; 916: 116384. <https://doi.org/10.1016/j.jelechem.2022.116384>
- [38] Ganguly A, Nath SS. Mn-doped CdS quantum dots as sensitizers in solar cells. *Materials Science and Engineering: B* 2020; 255: 114532. <https://doi.org/10.1016/j.mseb.2020.114532>

- [39] Zou X, He S, Teng G, Zhao C. Performance study of CdS/Co-doped-CdSe quantum dot sensitized solar cells. *Journal of Nanomaterials* 2014; 2014: 50-50. <https://doi.org/10.1155/2014/818160>
- [40] Meng X, Zhang C, Dong C, Sun W, Ji D et al. Carbon quantum dots assisted strategy to synthesize Co@NC for boosting photocatalytic hydrogen evolution performance of CdS. *Chemical Engineering Journal* 2020; 389: 124432. <https://doi.org/10.1016/j.cej.2020.124432>
- [41] Thambidurai M, Muthukumarasamy N, Velauthapillai D, Agilan S, Balasundaraprabhu R. Structural, optical, and electrical properties of cobalt-doped CdS quantum dots. *Journal of Electronic Materials* 2012; 41: 665-672. <https://doi.org/10.1007/s11664-012-1900-5>
- [42] Liu B, Aydil ES. Growth of oriented single-crystalline rutile TiO<sub>2</sub> nanorods on transparent conducting substrates for dye-sensitized solar cells. *Advanced Energy Conversion* 2009; 3 (2), 455-479. <https://doi.org/10.1021/ja8078972>
- [43] Chen J, Song W, Hou H, Zhang Y, Jing M et al. Ti<sup>3+</sup> Self-Doped Dark Rutile TiO<sub>2</sub> Ultrafine Nanorods with Durable High-Rate Capability for Lithium-Ion Batteries. *Advanced Functional Materials* 2015; 25 (43); 6793-6801. <https://doi.org/10.1002/adfm.201502978>
- [44] Chen H, Fu W, Yang H, Sun P, Zhang Y et al. Photosensitization of TiO<sub>2</sub> nanorods with CdS quantum dots for photovoltaic devices. *Electrochimica Acta* 2010; 56 (2), 919-924. <https://doi.org/10.1016/j.electacta.2010.10.003>
- [45] Pan Z, Qiu Y, Yang J, Liu M, Zhou L et al. Synthesis of three-dimensional hyperbranched TiO<sub>2</sub> nanowire arrays with significantly enhanced photoelectrochemical hydrogen production. *Journal of Materials Chemistry A*, 2015; 3 (7): 4004-4009. <https://doi.org/10.1039/c4ta06498d>
- [46] Muthalif MPA, Lee YS, Sunesh CD, Kim HJ, Choe Y. Enhanced photovoltaic performance of quantum dot-sensitized solar cells with a progressive reduction of recombination using Cu-doped CdS quantum dots. *Applied Surface Science* 2017; 2 (396): 582-589. <https://doi.org/10.1016/j.apsusc.2016.10.200>
- [47] Gopi CVVM, Venkata-Haritha M, Kim SK, Kim HJ. A strategy to improve the energy conversion efficiency and stability of quantum dot-sensitized solar cells using manganese-doped cadmium sulfide quantum dots. *Dalton Transactions* 2015; 44 (2): 630-638. <https://doi.org/10.1039/c4dt03063j>
- [48] Janbandhu SY, Munishwar SR, Sukhadeve GK, Gedam RS. Effect of annealing time on optical properties of CdS QDs containing glasses and their application for degradation of methyl orange dye. *Materials Characterization* 2019; 152: 230-238. <https://doi.org/10.1016/j.matchar.2019.04.027>
- [49] Yadav AN, Kumar R, Jaiswal RK, Singh AK, Kumar P et al. Surface modification of CdS quantum dots: An effective approach for improving biocompatibility. *Materials Research Express* 2019; 6 (5): 055002. <https://doi.org/10.1088/2053-1591/aaff70>
- [50] Gao X, Liu X, Zhu Z, Wang X, Xie Z. Enhanced photoelectrochemical and photocatalytic behaviors of MFe<sub>2</sub>O<sub>4</sub> (M = Ni, Co, Zn and Sr) modified TiO<sub>2</sub> nanorod arrays. *Scientific Reports* 2016; 6 (1): 30543. <https://doi.org/10.1038/srep30543>
- [51] Schreder B, Dem C, Schmitt M, Materny A, Kiefer W et al. Raman spectroscopy of II-VI semiconductor nanostructures: CdS quantum dots. *Journal of Raman Spectroscopy* 2003; 34 (2): 100-103. <https://doi.org/10.1002/jrs.959>
- [52] Nel JM, Gaigher HL, Auret FD. Microstructures of electrodeposited CdS layers. *Thin Solid Films* 2003; 436 (2): 186-195. [https://doi.org/10.1016/S0040-6090\(03\)00570-4](https://doi.org/10.1016/S0040-6090(03)00570-4)
- [53] Bendjama M, Hamdaoui O, Ferkous H, Alghyamah A. Removal of Safranin O from Water by UV/TiO<sub>2</sub>/IO<sub>3</sub><sup>-</sup> Advanced Oxidation Process: Parametric Study and Impact of Inorganic Ions and Humic Acid. *Catalysts* 2023; 13 (2): 447. <https://doi.org/10.3390/catal13020447>
- [54] Muruganandam S, Parivathini K, Murugadoss G. Effect of co-doped (Ni<sup>2+</sup>/Co<sup>2+</sup>) in CdS nanoparticles: investigation on structural and magnetic properties. *Applied Physics A* 2021; 127 (6): 400. <https://doi.org/10.1007/s00339-021-04555-0>
- [55] Murugesan R, Sivakumar S, Karthik K, Anandan P, Haris M. Effect of Mg/Co on the properties of CdS thin films deposited by spray pyrolysis technique. *Current Applied Physics* 2019; 19 (10): 1136-1144. <https://doi.org/10.1016/j.cap.2019.07.008>
- [56] Shah SA, Khan I, Yuan A. MoS<sub>2</sub> as a Co-Catalyst for Photocatalytic Hydrogen Production: A Mini Review. *Molecules* 2022; 27 (10): 3289. <https://doi.org/10.3390/molecules27103289>
- [57] Huerta-Flores AM, Chávez-Angulo G, Carrasco-Jaim OA, Torres-Martínez LM, Garza-Navarro MA. Enhanced photoelectrochemical water splitting on heterostructured α-Fe<sub>2</sub>O<sub>3</sub>-TiO<sub>2</sub>:X (X = Co, Cu, Bi) photoanodes: Role of metal doping on charge carrier dynamics improvement. *Journal of Photochemistry and Photobiology A: Chemistry* 2021; 410: 113077. <https://doi.org/10.1016/j.jphotochem.2020.113077>
- [58] Dey KK, Gahlawat S, Ingole PP. BiVO<sub>4</sub> optimized to nano-worm morphology for enhanced activity towards photoelectrochemical water splitting. *Journal of Materials Chemistry A* 2019; 7 (37): 21207-21221. <https://doi.org/10.1039/c9ta07353a>
- [59] Braiek Z, Ben Naceur J, Jrad F, Ben Assaker I, Chtourou R. Novel synthesis of graphene oxide/In<sub>2</sub>S<sub>3</sub>/TiO<sub>2</sub> NRs heterojunction photoanode for enhanced photoelectrochemical (PEC) performance. *International Journal of Hydrogen Energy* 2022; 47 (6): 3655-3666. <https://doi.org/10.1016/j.ijhydene.2021.10.268>
- [60] Gao XF, Sun WT, Ai G, Peng LM. Photoelectric performance of TiO<sub>2</sub> nanotube array photoelectrodes cosensitized with CdS/CdSe quantum dots. *Applied Physics Letters* 2010; 96 (15): 153104. <https://doi.org/10.1063/1.3386525>
- [61] Orimolade BO, Koiki BA, Peleyeju GM, Arotiba OA. Visible light driven photoelectrocatalysis on a FTO/BiVO<sub>4</sub>/BiOI anode for water treatment involving emerging pharmaceutical pollutants. *Electrochimica Acta* 2019; 307: 285-292. <https://doi.org/10.1016/j.electacta.2019.03.217>